J Electroceram (2007) 18:13–24
DOI 10.1007/s10832-007-9003-z

Microstructure analysis of the Y5V multilayer ceramic capacitors based on $BaTiO_3$

Yu-Chuan Wu · Jheng-Syun Lee · Hong-Yang Lu · Ching-Li Hu

Received: 1 December 2004 / Accepted: 23 May 2006 / Published online: 21 February 2007

Abstract The Y5V-1206 base-metal electrode (BME) multilayer ceramic capacitor (MLCC) chips have been characterised for crystalline phases using X-ray diffractometry (XRD), and microstructure using optical microscopy (OM), scanning electron microscopy (SEM) and transmission electron microscopy (TEM). The microstructure features found in the Ni electrode and the $BaTiO_3$ dielectric layer are discussed in terms of the tensile backstresses induced upon firing due to constrained sintering heterogeneously. The chemical compositions containing BaO-excess and additives CaO and ZrO_2, determined for $BaTiO_3$ grains by energy-dispersive spectroscopy (EDS) equipped in the TEM are also reported. However, no rare-earth oxides were found in the grains. The representative microstructure of $BaTiO_3$ grains containing dislocations is the "solid-solution" type distinctive from the "core-shell" of the X7R compositions. The fact that no ferroelectric domains were detected suggests that the $BaTiO_3$ grains are pseudo-cubic with the c/a ratio ≈ 1.0.

Keywords $BaTiO_3$ · Dielectrics · MLCCs · TEM · Sintering

1 Introduction

For achieving higher capacitance (C) in a small volume, the number of the dielectric layers in MLCC's is increased when overall dimension reduced (from 1206 to 0603, to 0402) [1] as described by:

$$C = n\varepsilon_o\varepsilon_r A/d \quad (1)$$

where n: number of dielectric layers, ε_o: permittivity in vacuum, ε_r: relative permittivity (or dielectric constant), A: total planar area, and d: thickness of a dielectric layer.

Two approaches have been taken to improve the dielectric behaviour of MLCC's towards higher capacitance, longer life time and higher reliability to meet the increasing demand of miniaturisation to a denser degree. The first alters the chemical composition of the $BaTiO_3$-based dielectric layer to refine the microstructure [2]. Oxygen vacancies, suggested [3] to have a detrimental effect on the reliability and life time of dielectrics based on $BaTiO_3$, may be reduced if the ceramic is added with donors, often the rare-earth metal oxides [4], by which the composition (and so the defect structure) is modified. The other improves the processing technology, particularly of $BaTiO_3$ film casting, liquid-phase-sintering additives, and particle-size distribution of the paste for Ni electrodes.

The permittivity of $BaTiO_3$ single-crystal varying from ε_a=400 along ⟨100] to ε_c=4,000 along [001] is anisotropic [2]. Undoped $BaTiO_3$ ceramics have ε_r lying between 2,000 to 6,000, with an average grain size (G_{av}) several micrometres to several tens. Commercially, the compositions of reducible dielectrics for making BME-MLCC's differ considerably [5] by the selected additives. Dopant systems combining the rare-earth metal oxides, e.g., La_2O_3, Nd_2O_3, Sm_2O_3, Gd_2O_3, Dy_2O_3, Ho_2O_3, and Er_2O_3 with MgO (and ZrO_2) (of < 0.2 at.%) are adopted and 0.5 wt.% Li_2O–SiO_2–CaO glass is also added for promoting densification by liquid-phase sintering [5]. Based on such formulations, desirable dielectric properties have been developed successfully, particularly with improved life time [4–6]. Rare-

Y.-C. Wu · J.-S. Lee · H.-Y. Lu (✉)
Centre for Nanoscience, Institute of Materials Science and Engineering, National Sun Yat-Sen University, Kaohsiung 80424, Taiwan
e-mail: hyl@mail.nsysu.edu.tw

C.-L. Hu
R&D Technology Centre, Yageo Corporation Nan-Tze Branch, Kaohsiung 811, Taiwan

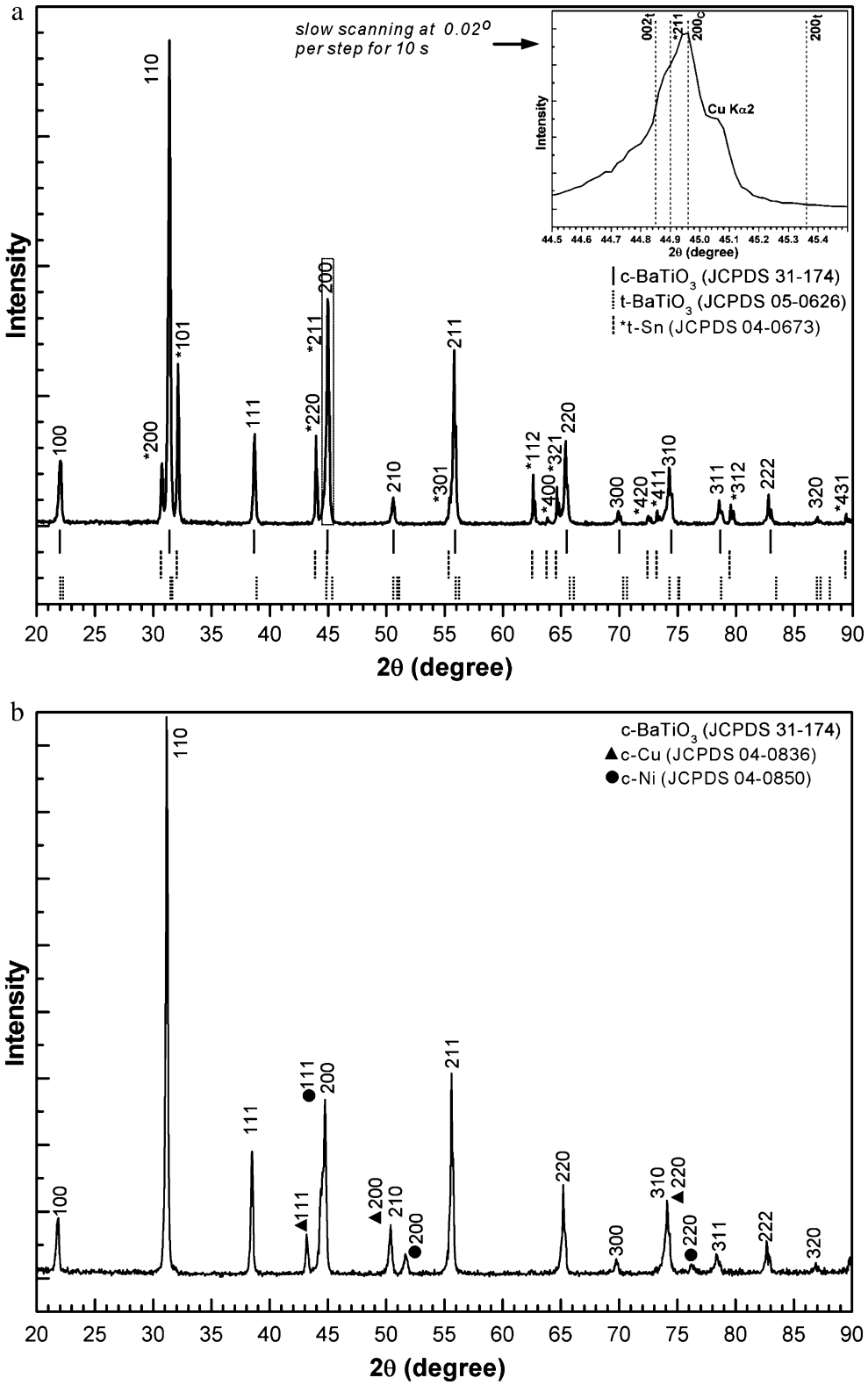

Fig. 1 XRD traces of **a** as-received, with the slow scanning of {002} peak shown inset, and **b** polished MLCC chips

earth cations, e.g., Y^{3+} [7, 8] substituting for both the A-and B-site depending [4–6] on the concentration, processing conditions, e.g., oxygen partial pressure, and sintering temperature, being amphoteric [4–6], play a dual role of being donor (donating electrons) and acceptor (generating oxygen vacancies) simultaneously.

Microstructure analysis for $BaTiO_3$-based ceramics has been concentrated on sintered samples [9–15]. Although the

interface of Ni-electrode and $BaTiO_3$ dielectric layer of a Y5V composition was studied for interdiffusion [16], very rarely were the microstructure of commercial MLCC chips investigated under TEM for improving the manufacturing process that is known to require high precision, to be complicated, and sensitive to many unidentified parameters [18]. Residual pores in the Ni electrode layers have often been found in almost all MLCC chips, but its origin was not fully understood. We have chosen to analyse the crystalline phases, microstructure using XRD, SEM and TEM for commercial Y5V BME-MLCC chips for its dielectric behaviour and grain microstructure being characteristically distinctive from those of the X7R formulation. Representative microstructures of the internal and external electrodes, interface, and dielectric layers are reported here. The results would be beneficial for making better performance and more reliable MLCC chips.

2 Experimental procedure

The Y5V-1206 MLCC chips of ~3.20×1.60 mm (0.120×0.060 in) in size [1] and rated 1 μF were manufactured by Yageo Co. Nan-Tze Branch (Kaohsiung, Taiwan). The chips are $BaTiO_3$-based with both A- and B-site isovalent additives, i.e., $CaZrO_3$ and $BaZrO_3$, having an average grain size G_{av}=3–10 μm, according to EIA specifications.

Crystalline phases were determined with XRD (D-5000 diffractometer, Siemens, Karshrule, Germany) using Cu kα radiation operating at 40 kV/30 mA with Ni filter using a 0.2 mm receiving slit. Chips were ground using SiC grits and polished with diamond pastes on a Streuer (Copenhagen, Denmark) lapping machine successively to 1 μm surface roughness. Polished samples were then chemical-etched in a 30% HCl solution added with a few drops of HF to delineate grain boundaries, and other microstructure features. Observations were made in a reflected light OM (Nikon, Tokyo, Japan) and an SEM JEOL™ 6400 (Tokyo, Japan) operating at 20 kV and equipped with energy-dispersive X-ray spectroscopy (EDS, Link Systems, Oxford, England).

Thin foils for TEM were prepared by the conventional technique of stacking several chips together in epoxy resin, cutting with a diamond-embedded saw, ultrasonic-drilling to discs of 3 mm in diametre, then grinding and polishing to ~30 μm thick and 1 μm surface roughness before dimple-grinding to ~10 μm thick in the centre region. The thin sections were then Ar-ion-beam thinned to electron transparency. Observations and chemical analysis were made in a JEOL™ AEM3010, equipped with EDS (Link Systems) and a double-tilting stage of ±45° for the x-tilt and ±30° for the y-tilt, operating at 300 kV.

3 Results

3.1 Crystalline phases-XRD

As-received sample surface and polished surface were both analysed by XRD. Figure 1 shows predominantly cubic (c)-$BaTiO_3$ (JCPDS 31-0174) from the dielectric layers and Sn (JCPDS 4-0673) from the external electrodes. Although no apparent peak splitting was discerned (trace (a) in Fig. 1), slow scanning of $2\theta = 44.5 - 45.5°$ at 0.02° per step for 10 s revealed a non-Gaussian peak consisting of $\{200\}_{pc}$ (where pc for pseudo-cubic) and $\{211\}_{Sn}$ at $2\theta \approx 44.90 - 44.96°$, as shown inset. Polished surface also revealed internal BME's consisting of Ni (JCPDS 4-0850) and Cu (JCPDS4-0836), as indicated in trace (b).

3.2 General microstructure-OM and SEM

Both top view and cross-section delineating the dielectric layer, the external as well as internal electrodes are shown, respectively, in Fig. 2a and b, assembled from a number of images. The $BaTiO_3$-based dielectric of 45 layers may be counted directly from the cross-section view (Fig. 2b). Each $BaTiO_3$-based dielectric layer is approximately 7.5 μm and each Ni electrode layer ~2 μm thick. Since surface polishing on a lapping machine was not performed exactly parallel to the Ni-electrodes, the electrode layers appeared as ripples (Fig. 2a) across the polished surface.

Figure 3a shows the top view under OM, revealing the interface between external and internal electrodes. A thin layer Ni-electrode, indicated by filled arrow, was sandwiched between Sn and Cu. Inter-diffusion between Ni, Cu

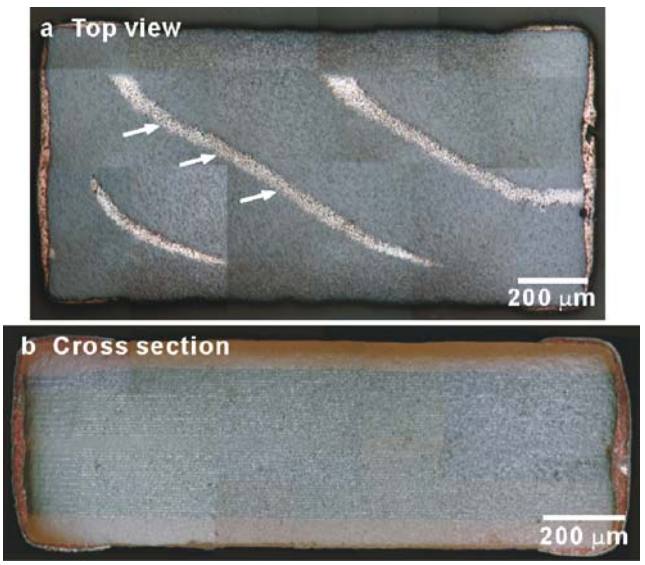

Fig. 2 **a** Top, and **b** cross-section views of Y5V MLCC (OM)

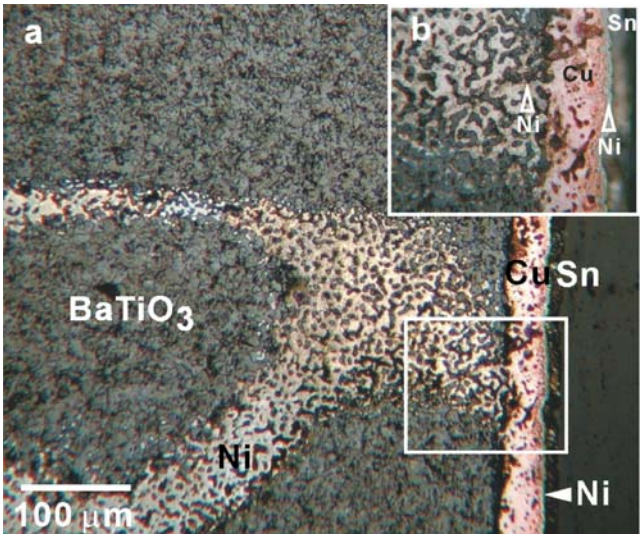

Fig. 3 Inter-diffusion of Ni–Cu shown by light reflectivity under OM

and Ni (i.e. Ni–Cu–Ni) as indicated in Fig. 3b, has occurred at the electrode interfaces forming Ni–Cu alloys [19]. This is registered by light reflectivity changing across the interface, as indicated by unfilled arrows. The Cu electrode contained many residual pores (Fig. 3a). Interfacial crack-like voids between $BaTiO_3$ dielectric layer and Cu electrode are also discerned. Extensive (particle) coarsening occurred in both Cu and Ni electrodes upon sintering is unambiguous. Thus, a significant proportion of the dielectric layer would have lost electrical contact with the electrodes. SEM combined with EDS, given in Fig. 4, although at a different location, has confirmed the existence of a thin Ni-layer and the inter-diffusion forming Ni–Cu solid solution (indicated in Fig. 4d for Cu) shown by OM in Fig. 3a and b.

The Cu electrode containing residual pores from incomplete sintering is better discerned from a cross-section view shown in Fig. 5a. The Sn–Ni boundary can be differentiated from SEM-secondary electron image (SEI). Crack-like pores at the interface between Cu-electrode and $BaTiO_3$-dielectric layer would have resulted in poor (electrical) contact. The $BaTiO_3$ grain boundaries in the vicinity of Cu-electrode etched away (as arrowed), are clearly visible. This suggests the grain boundaries close to the Cu electrode is of an amorphous nature. However, no ferroelectric domains were detected from the $BaTiO_3$ grains. Twinning along {111} is occasionally found [20–22, 37], both single [20, 21, 37] and double twins [20, 21, 37], as indicated by unfilled arrows in Fig. 5a. Double twins can be easily distinguished by a thin slab [22, 37] running across $BaTiO_3$ grains. Facetted grain boundaries [10, 11], shown by unfilled arrows, suggest a glassy phase that has been etched away.

Figure 5b shows a general microstructure of the $BaTiO_3$ dielectric layer. Rounded grain corners at triple-grain junctions indicate liquid-phase-assisted sintering. An average grain size of $BaTiO_3$ ceramic in the range of ~3–5 μm was estimated. However, no second-phases, e.g., glassy grain-boundary phase [10, 13], $Ba_6Ti_{17}O_{40}$ [10], were immediately discernible.

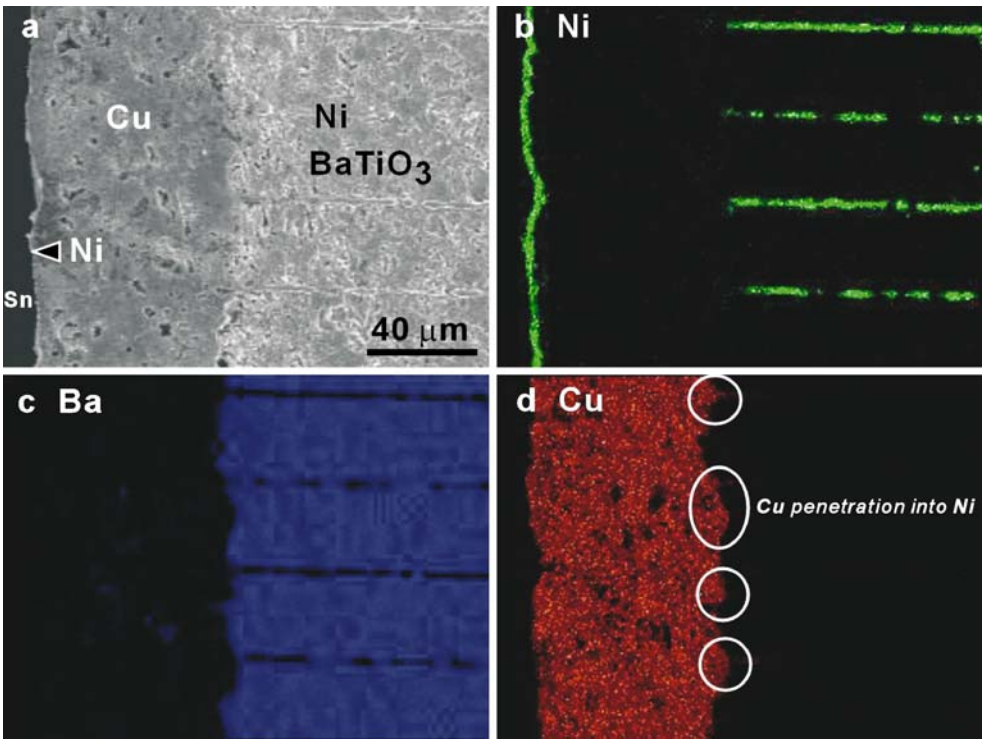

Fig. 4 **a** Interface of Ni–Cu–Ni (SEI–SEM) and **b**, **c** and **d** EDS spectra indicating inter-diffusion

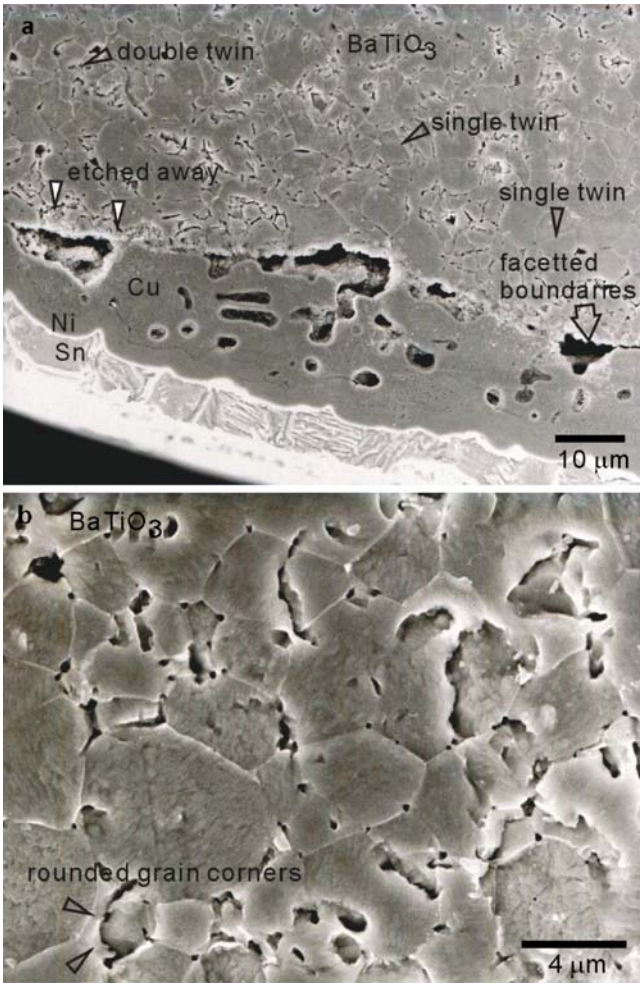

Fig. 5 **a** Cross-section view of Sn, Ni and Cu showing residual pores and crack-like pores at interface, and **b** general microstructure of $BaTiO_3$ layer (SEI–SEM)

None of the Ni electrodes shown in Fig. 2a and b was a continuous layer. A top view under SEM (Fig. 6a) indeed confirmed the OM observation that the Ni layer has undergone extensive particle coarsening without significant densification. That has resulted in discontinuous Ni grains in the electrode (Fig. 6b). Nevertheless, both the thickness of the dielectric layer and Ni electrode are rather uniform. Therefore, each dielectric layer [17], between Ni electrodes, contains approximately two to three $BaTiO_3$ grains [18].

3.3 TEM analysis

3.3.1 $BaTiO_3$ dielectric layer

Tilting the foil to Z=[100], spot splitting [12, 13] along [011] representing the tetragonality was not detected. This suggests that the sintered $BaTiO_3$ grains consistent with XRD trace (referred to Fig. 1a) are (pseudo-)cubic in symmetry, as shown in Fig. 7a with corresponding SADP in Fig. 7b. Dislocations are also found, as indicated, which are most likely to be perfect with the Burgers vector $b = \langle 1\bar{1}0 \rangle$ [23, 24]. It is because the slip systems of $\langle 1\bar{1}0 \rangle \{110\}$, detected in scratched samples, were also produced by high-temperature deformation [23]. Sintering can be perceived as if the ceramic powder compact was undergoing plastic deformation by a hydrostatic compressive stress at high temperatures.

The $\{1\bar{1}1\}$ single twins (Fig. 5a), unlike $BaTiO_3$ sintered at low temperatures (≈1,250°C [20, 21]), were observed only occasionally. Both parts (i.e., A and B) of the twin-grain appear in different contrast due to a slight deviation from the Bragg position registered by the ***g***-vectors [25], i.e., $\Delta g = g_A - g_B$, due to obliquity. Figure 8a shows a bright-field (BF) image with corresponding SADP's in Fig. 8b where the diffraction aperture was placed in crystal part A, interface, and crystal part B, respectively. This is an interface of the coincident-site lattice (CSL) with Σ=3 [14], both the fault vector [15, 37]

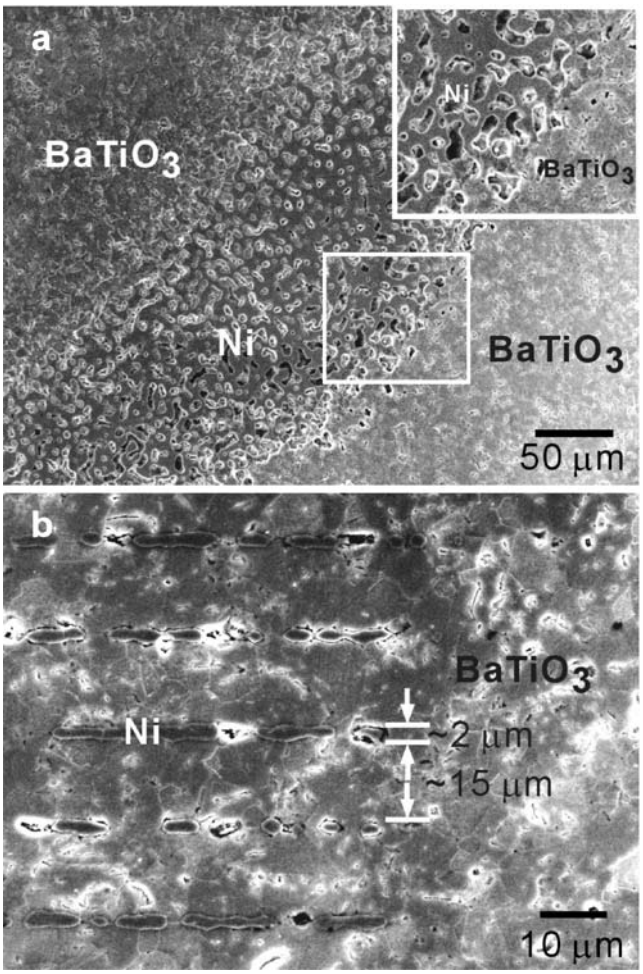

Fig. 6 **a** Top view of Ni electrode showing coarsening, and **b** cross-section view showing discontinuous Ni-electrode layer (SEI–SEM)

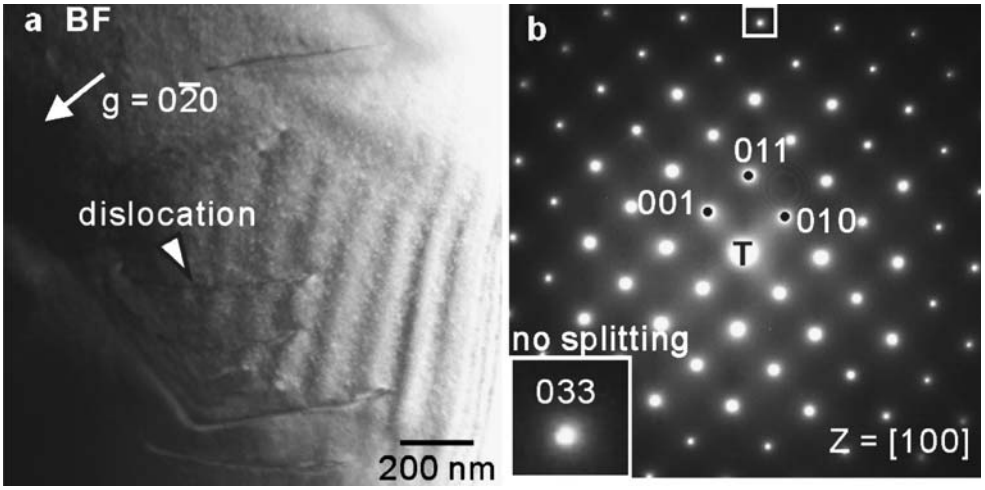

Fig. 7 **a** Representative microstructure of pseudo-cubic $BaTiO_3$ with **b** the corresponding SADP juxtaposed (BF image-TEM)

$R = 1/3\langle 1\bar{1}2\rangle$ and transformation matrix [14, 37] have previously been determined experimentally by others.

Double twinning [21, 22, 37] is shown in Fig. 9a with the corresponding SADP's in Fig. 9b where parallel zone axes $[2\bar{2}1]//[001]$ in consistent with the crystallographic orientation relationships determined [37] for the {111} single twins are again obtained. Interfacial dislocations probably lying in twin boundaries [15, 26] are indicated.

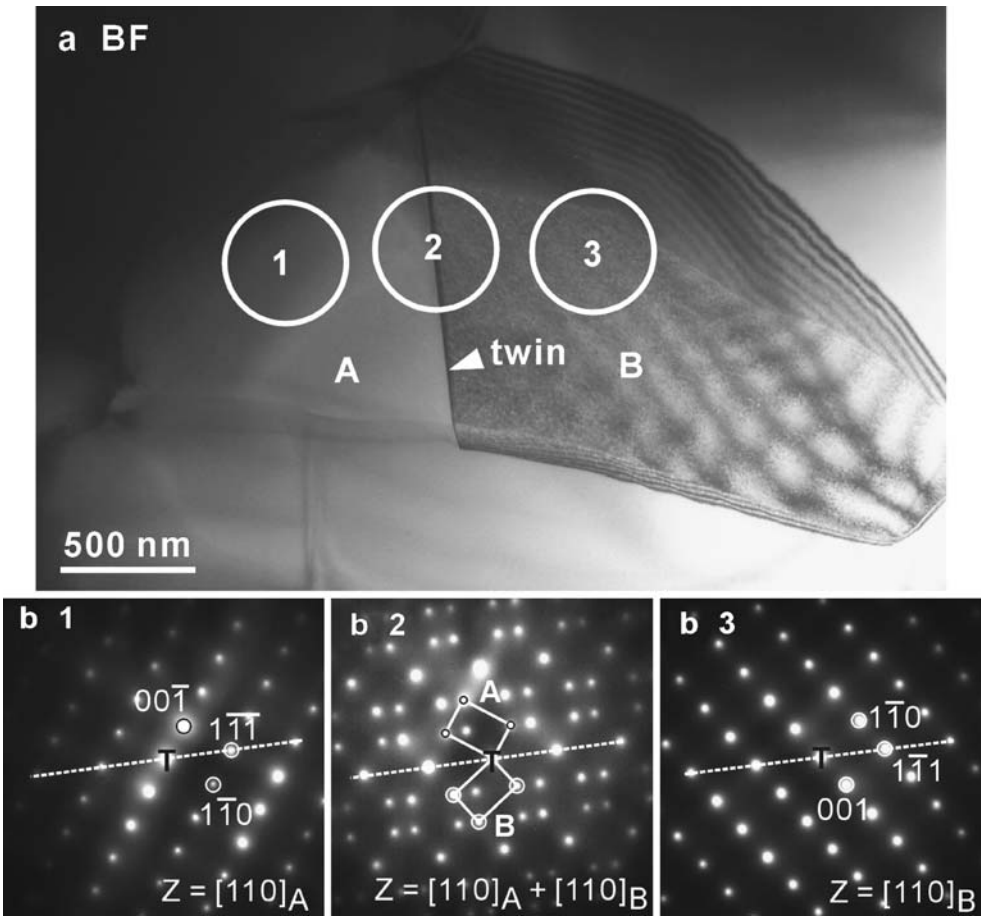

Fig. 8 Single twinning on {111} **a** BF image with **b** the corresponding SADP's

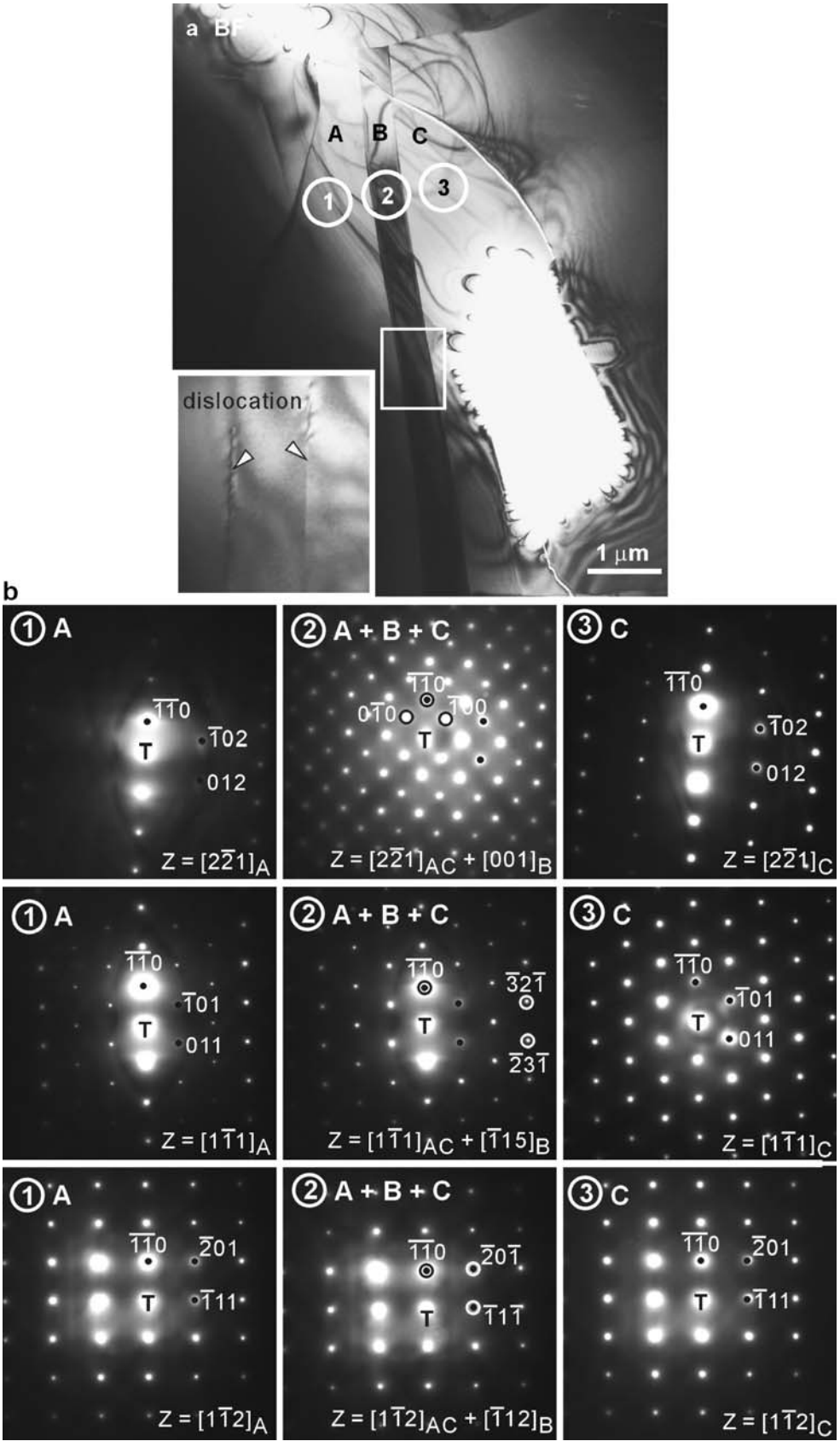

Fig. 9 Double twin lamella showing the corresponding SADP's and the interfacial dislocations (BF image-TEM)

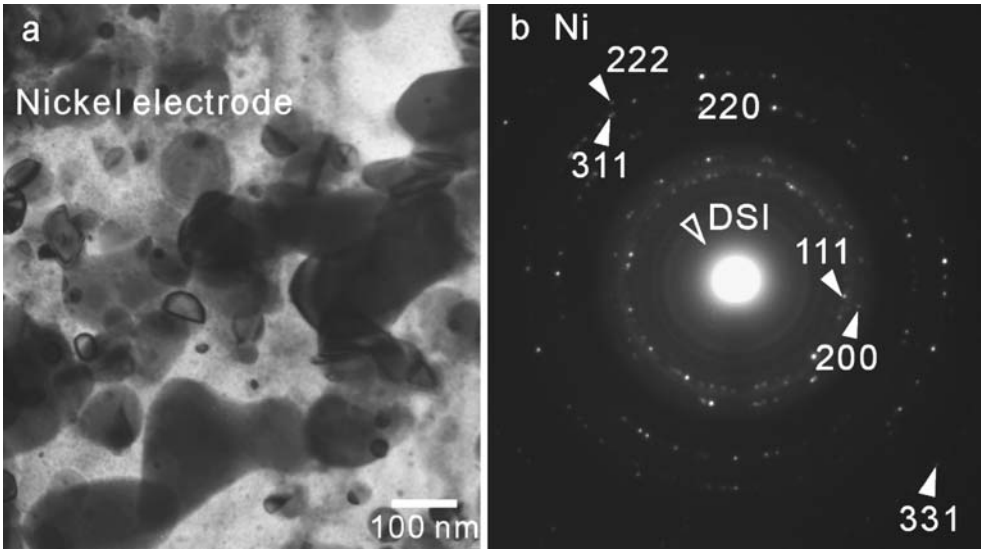

Fig. 10 **a** Coarsened Ni-electrode with **b** the corresponding SADP showing an amorphous background (BF image-TEM)

3.3.2 Nickel electrodes

Several morphologies of the Ni-electrode layer have been observed. Relatively large Ni particles, several hundreds of nanometres, showing necking were poorly sintered. The corresponding SADP (Fig. 10b) containing diffuse scattering intensity (DSI) suggests an amorphous background in Fig. 10a. A continuous layer of Ni electrode with an average grain size of ~100 nm was observed and shown in Fig. 11a with a higher magnification in Fig. 11b. The fact that no residual pores were found suggests a fully densified Ni-layer. Some electrode layers, however, are highly porous (Fig. 12a). The Ni-particles were coarsened, as indicated in framed region when no apparent orientation relationship between Ni and $BaTiO_3$ could be distinguished. The Ni-electrode layer containing an amorphous phase is again shown by DSI in Fig. 12e.

3.3.3 Chemical compositions

$BaTiO_3$ grains did not exhibit the characteristic ferroelectric domains [9–13]. Such a featureless grain, similar to the shell region of X7R's, is sometimes referred to as the "solid-solution" in contrast to the "core-shell" of the X7R compositions [9, 17]. A representative microstructure of $BaTiO_3$ grains is shown in Fig. 13a with its higher magnification juxtaposed (Fig. 13b). Glassy phases located at triple-grain junctions are easily discerned. Their existence along with rounded grain corners, as indicated, often found with MLCC's [27], is diagnostic of a liquid-phase-assisted

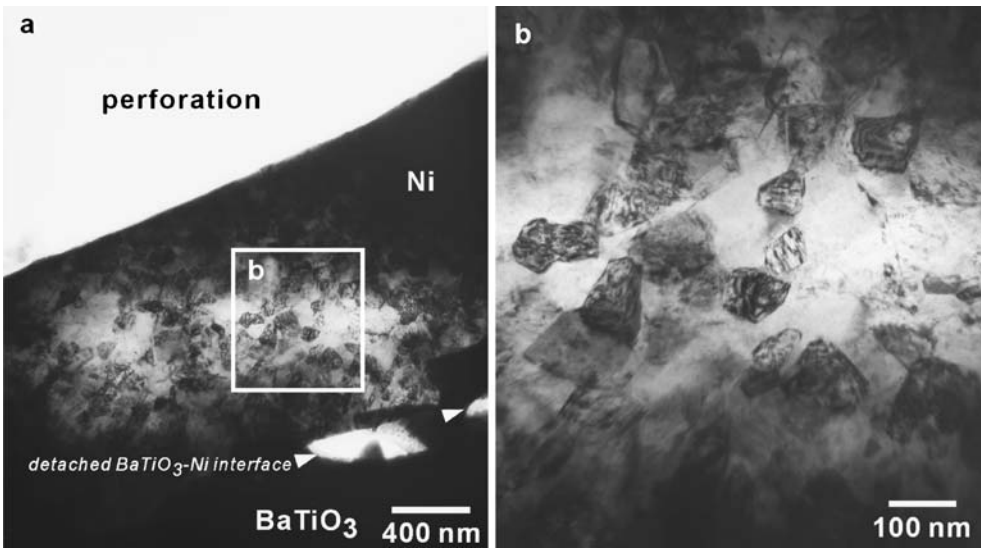

Fig. 11 A continuous layer of Ni electrode of average grain size ~100 nm (BF image-TEM)

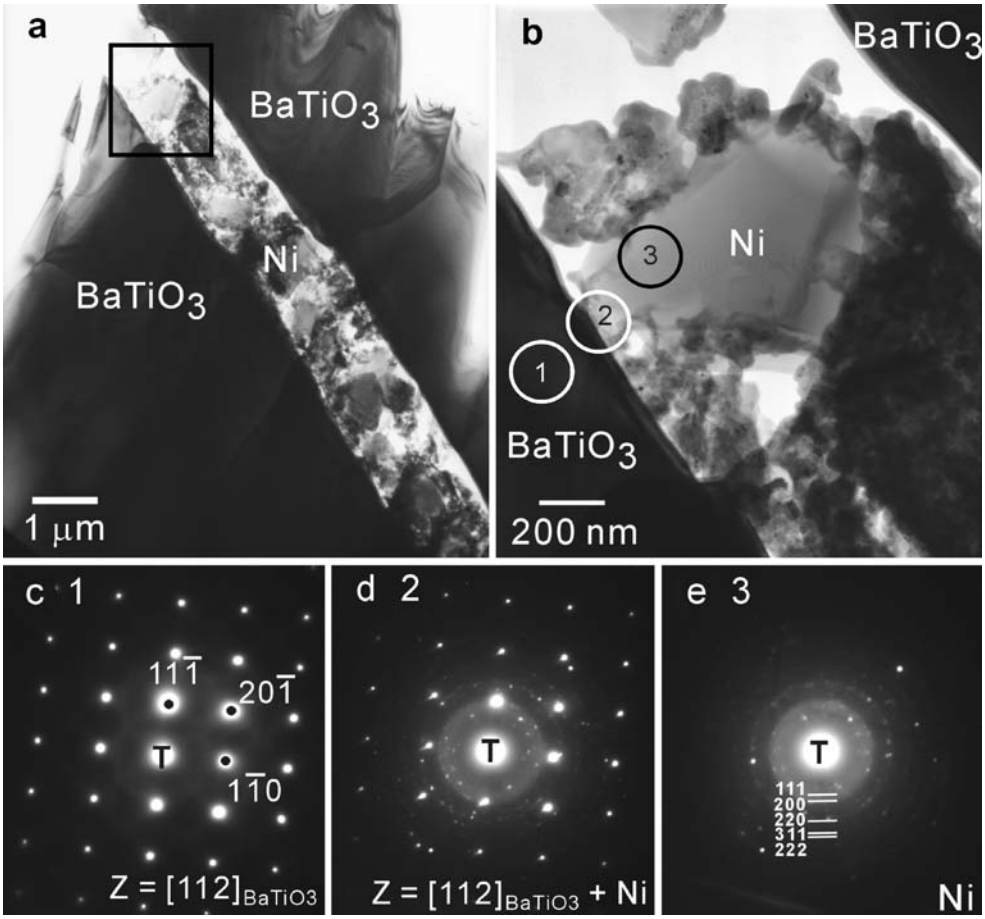

Fig. 12 **a** Porous Ni-electrode, and **b** higher magnification showing **c**, **d** no specific orientation relationships with $BaTiO_3$ grain substrate and **e** an amorphous background (BF image-TEM)

sintering mechanism. Dislocations (indicated by filled arrows) are visible, although not determined for the Burgers vectors. The speckles on grain surface are the relics of Ni electrode from ion-beam thinning during foil preparation.

Two such grains were analysed for the contents of Ba, Ca, Ti, and Zr. Results are given in Fig. 14a and b with the corresponding EDS data listed in Table 1a and b. All elements are homogeneously distributed across grains. The

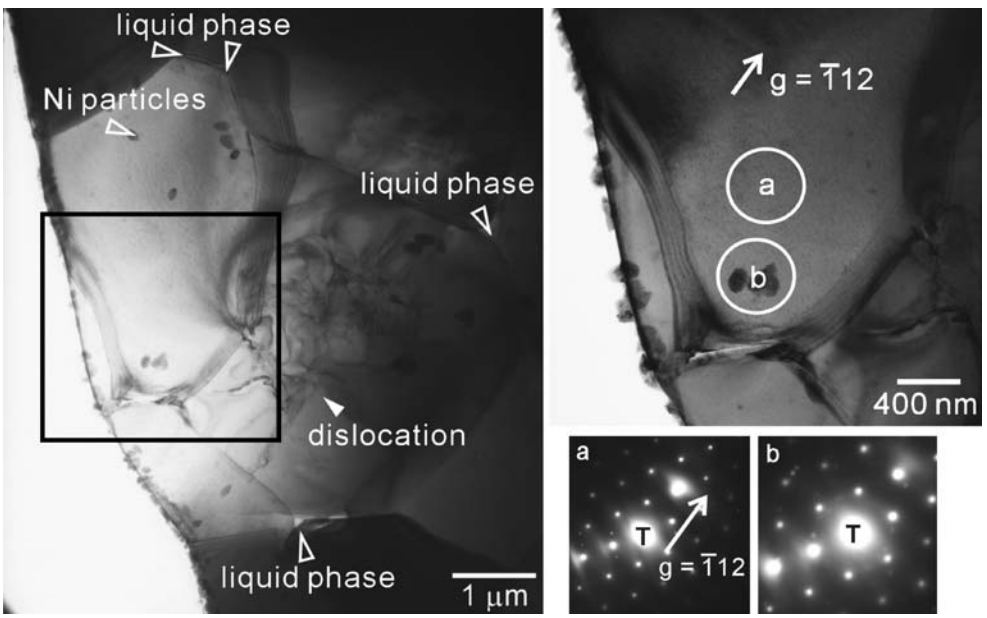

Fig. 13 **a** Representative microstructure of $BaTiO_3$ grains containing dislocations and showing the "solid-solution" type and glassy phase at triple-grain junctions, with **b** higher magnification juxtaposed (BF image-TEM)

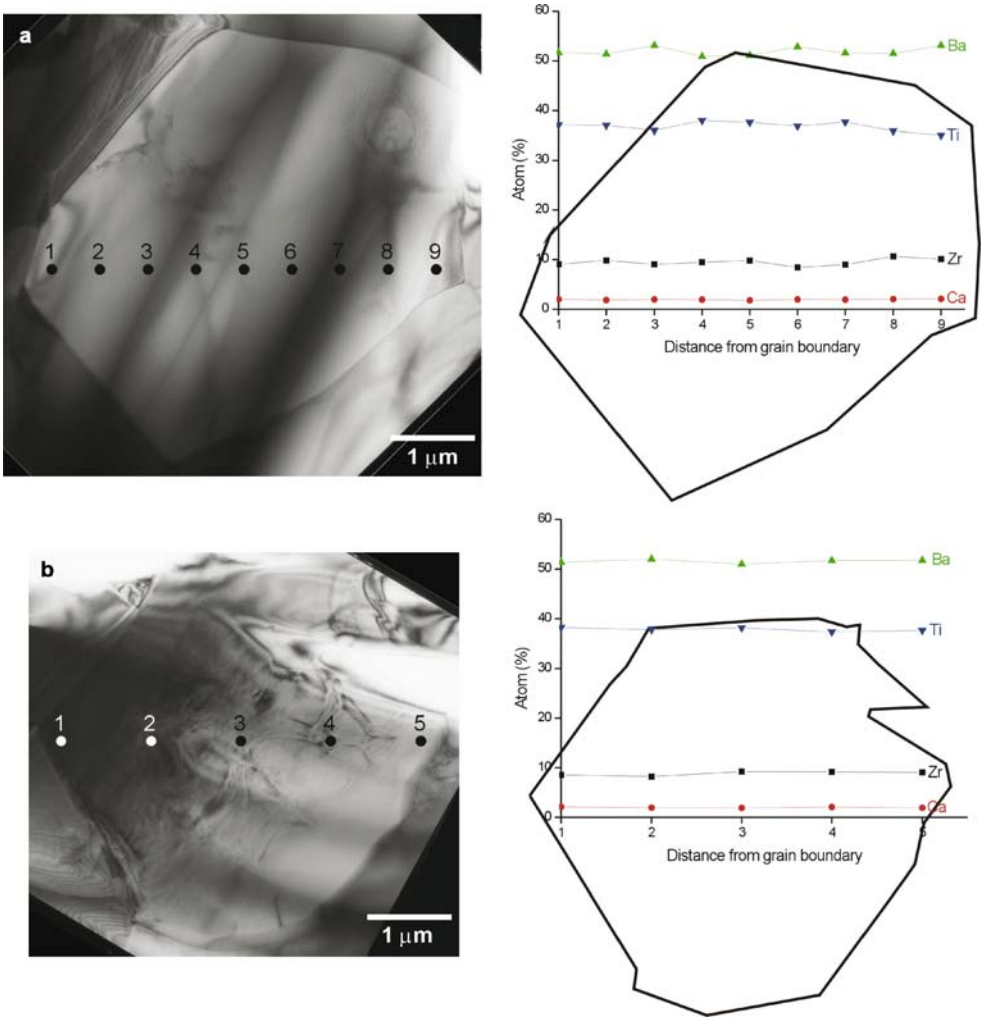

Fig. 14 Chemical analysis showing the distribution of elements, Ba, Ti, Ca, and Zr for two $BaTiO_3$ grains, (**a**) and (**b**)

average Ba/Ti-ratios of 1.059 and 1.080 are both BaO-excess, are calculated by assuming that both Ca^{2+} [28, 29], Zr^{4+} substitutes for Ti^{4+} [9].

4 Discussion

Starting $BaTiO_3$ powders for BME-MLCC are usually A-site excess having the Ba/Ti-ratio between 1.000 and 1.005 [27, 29, 38]. Here, even if Ca^{2+}, of a few atomic percent [29], all substituted for the Ti-site, we still have the grain compositions of BaO-excess with the Ba/Ti-ratios of 1.059 and 1.080 that have well exceeded the typical range reported [5] in the literature. The fact that rare-earth cations were not detected is inconsistent with the Y5V compositions reported by Kishi et al. [5]. The cause of that is not certain from the present results.

Although processed in a reducing atmosphere, dislocation loops usually found [30, 38] to condense on the {011} domain boundaries [38] in X7R's [27, 38] were not detected. Further, the fact that ferroelectric domains were not observed in the $BaTiO_3$ grains (e.g., Fig. 13) is consistent with the XRD results (Fig. 1). This suggests that the grains are predominantly pseudo-cubic with the c/a ratio ≈ 1.0. The representative microstructure of the so-called "solid-solution" in Y5V (Fig. 13) is distinctive from the "core-shell" microstructure [9] found in the X7R compositions [5, 17]. Whether the microstructure may account for the difference in the dielectric permittivity of the two formulations of Y5V and X7R requires further study to be certain.

Sandwiched and confined between $BaTiO_3$ dielectric layers, some of the Ni electrodes sintered rather well (Fig. 11), but some did not (Figs. 11 and 12). Constrained sintering [31–34] is known to occur due to the backstresses developed in a powder compact of inhomogeneous green density. The inhomogeneities in green bodies may have been loose soft agglomerates or hard inclusions [32–34], but they all develop crack-like voids [31] in the proximity with the matrix grains due to differential sintering rates. Consider for spherical agglomerates, soft agglomerates sintered at faster rates than the matrix generate radial tensile stresses; hard inclusions, however, being un-sinterable or sintered relatively slowly create tangential tensile stresses in the matrix.

Table 1 a and b EDS data for the distribution of Ba, Ti, Ca, Zr in two $BaTiO_3$ grains corresponding to Figs. 14a and b.

Atom (%)				
	Ba	Ti	Zr	Ca
a				
1	51.38	38.23	8.57	2.13
2	52.01	37.77	8.20	1.95
3	50.99	38.16	9.23	1.89
4	51.71	37.33	9.16	2.08
5	51.73	37.64	9.08	1.92
Av.	61.64	37.83	8.85	1.99
b				
1	51.66	37.09	9.08	2.02
2	51.38	37.01	9.86	1.86
3	53.10	36.10	9.06	1.98
4	50.90	37.98	9.47	1.94
5	51.10	37.61	9.83	1.83
6	52.38	36.85	8.43	1.98
7	51.60	37.68	9.00	1.94
8	51.48	35.90	10.65	2.06
9	53.10	35.06	10.10	2.10
Av.	51.86	36.86	9.50	1.97

Av: Average

Inhomogeneities in the green body of MLCC's may stem from two sources: one between $BaTiO_3$ dielectrics and Ni electrode, depending on the respective green density (and solid content in Ni), the other within the dielectrics and electrode themselves. The backstresses induced along the normal direction of the MLCC chips tend to pull the Ni layers apart, resulting in processing flaws [35], e.g., warpping, delamination, and cracking observed macroscopically. The backstresses developed between $BaTiO_3$ dielectric and Ni electrode, have retarded the densification of Ni electrodes, as shown in Fig. 12.

Tensile stress along the direction perpendicular to the electrode induced during firing has been reported [35], although the actual values of ~36 MPa to ~240–277 MPa varied considerably. Multiple delamination and cracks found in the MLCC's were attributed to the internal stresses induced during firing. The internal stresses [35] are in fact the backstresses developed from constrained sintering, acting in the opposite direction of the thermodynamic driving force (Δp), have hampered the densification of Ni electrode layer sandwiched between two $BaTiO_3$ dielectric layers (here, $BaTiO_3$–Ni–$BaTiO_3$ is taken as a unit for the sake of discussion). Microscopically, the coarsened Ni electrode (Figs. 3a, 6a and 10a) is representative of the broken pair-wise particle-chains [34, 36] which are being pulled apart by tensile backstresses developed along the chains when the matrix, i.e., $BaTiO_3$ dielectric layers, like the soft agglomerates [25–32], is being sintered at faster rates. The fact that some of the Ni electrode appeared better densified (Fig. 11) also indicates that the tensile backstresses are not uniformly distributed over the entire area of MLCC's. Therefore, an immediate suggestion of improving such flaws is to reduce the discrepancy of green density between $BaTiO_3$ and Ni layers during film casting and electroding.

5 Conclusions

We have analysed the microstructure of the commercial Y5V BME-MLCC's in which processing flaws in both the dielectric and electrode layers were found. Internal and external electrodes, Ni, Cu and Sn, are easily identified. Interfacial cracks between $BaTiO_3$ dielectric layer and Ni electrode, reducing the electrical contact, are evidenced from the microstructure. Tensile stresses developed during constrained sintering due to the inhomogeneities (of green density) between $BaTiO_3$ dielectric and Ni electrode, have resulted in inter-layer cracks. The $BaTiO_3$-based dielectric is of the pseudo-cubic symmetry having the c/a ratio ≈ 1.0. Its composition containing additives CaO and ZrO_2, is BaO-excess at the Ba/Ti-ratios of 1.059 and 1.080. Representative microstructure of the "solid-solution" type containing dislocations with no ferroelectric domains in the $BaTiO_3$ grains is distinctive from the "core-shell" type of X7R. If the microstructure discrepancy may account for the difference in the dielectric permittivity necessitates further study in conjunction with dielectric measurements.

Acknowledgement Thanks are due to the National Science Council of Taiwan for funding through contracts NSC 88-2216-E-110-009, 89-2216-E-110-037, 90-2216-E-110-018, 91-2216-E-110-017, 91-2216-E-110-018, and 92-2216-E-110-003.

References

1. G.R. Thomas, Am. Ceram. Soc. Bull. **80**, 29 (2001)
2. G. Arlt, D. Hennings, D. deWith, J. Appl. Phys. **58**, 1619 (1985)
3. R. Waser, T. Baiatu, K.H. Härdtl, J. Am. Ceram. Soc. **73**, 1645 (1990)
4. Y. Tsur, A. Hitomi, I. Scrymgeour, C.A. Randall, Jpn. J. Appl. Phys. **40**, 255 (2001)
5. H. Kishi, Y. Mizuno, H. Chazono, Jpn. J. Appl. Phys. **42**, 1 (2003)
6. Y. Tsur, C.A. Randall, in *Fundamental Physics of Ferroelectrics 2000*, ed. by R.E. Cohen (Am. Inst. Phys., 2000), p. 283
7. M.H. Lin, H.Y. Lu, Mater. Sci. Eng. A **335**, 101 (2002)
8. J. Zhi, A. Chen, Y. Zhi, P.M. Vilarinho, J.L. Baptista, J. Am. Ceram. Soc. **82**, 1345 (1999)
9. H.Y. Lu, J.S. Bow, W.H. Deng, J. Am. Ceram. Soc. **73**, 3562 (1990)
10. M.H. Lin, H.Y. Lu, Acta Mater. **50**, 605 (2002)
11. J.K. Liou, M.H. Lin, H.Y. Lu, J. Am. Ceram. Soc. **85**, 2931 (2002)
12. Y.H. Hu, H.M. Chan, X.W. Zhang, M.P. Harmer, J. Am. Ceram. Soc. **69**, 594 (1986)
13. Y.F. Chou, M.H. Lin, H.Y. Lu, Acta Mater. **48**(12), 3569–3579 (2000)

14. Y.C. Wu, *An Analysis of Defects in Metastably Retained Hexagonal $BaTiO_3$*, PhD Thesis, National Sun Yat-Sen University, Taiwan, 2004
15. O. Eibl, P. Pongratz, P. Skalicky, Philos. Mag., B **57**, 521 (1988)
16. Z.L. Gui, Y.L. Wang, L.T. Li, Ceram. Int. **30**, 1275 (2004)
17. F. Azough, R. Al-Saffar, R. Freer, J. Eur. Ceram. Soc. **18**, 751 (1998)
18. D.E. McCauley, K. Albersten, S.H. Chu, M.H. Megherhi, I. Hayashi, *Ferro BME MLCC Seminar*, Taipei, Taiwan, May 14, 2004
19. M. Hansen, *Constitution of Binary Alloys*, 2nd edn., (McGraw-Hill, N.Y., 1958)
20. H. Oppolzer, H. Schemlz, J. Am. Ceram. Soc. **66**, 444 (1983)
21. B.K. Lee, S.Y. Chung, S.J.L. Kang, J. Am. Ceram. Soc. **83**, 2858 (2000)
22. Y.K. Cho, D.Y. Yoon, J. Am. Ceram. Soc. **87**, 438 (2004)
23. N. Doukhan, N.C. Doukhan, Phys. Chem. Miner. **13**, 403 (1986)
24. M.H. Lin, H.Y. Lu, Mater. Sci. Eng. A **328**, 267 (2002)
25. S. Amelinckx, J. van Landuyt, in *Diffraction and Imaging Techniques in Materials Science*, ed. by S. Amelinckx, R. Gevers, J. van Lnaduyt (North-Holland, Amsterdam, The Netherlands, 1978), p.107
26. C. Metzmacher, K. Albersten, J. Am. Ceram. Soc. **84**, 821 (2001)
27. Y.H. Han, J.B. Appleby, D.M. Smyth, J. Am. Ceram. Soc. **70**, 96 (1987)
28. Y. Sakabe, Am. Ceram. Soc. Bull. **66**, 1338 (1987)
29. T. Suzuki, M. Ueno, Y. Nishi, M. Fujimoto, J. Am. Ceram. Soc. **84**, 200 (2001)
30. R. Raj, R.K. Bordia, Acta Metall. **32**, 1003 (1984)
31. O. Sudre, F.F. Lange, J. Am. Ceram. Soc. **75**, 519 (1992)
32. O. Sudre, F.F. Lange, J. Am. Ceram. Soc. **75**, 525 (1992)
33. O. Sudre, G. Bao, B. Fan, F.F. Lange, A.G. Evans, J. Am. Ceram. Soc. **75**, 3241 (1992)
34. Y.I. Shin, K.M. Kang, Y.G. Jung, J.G. Yeo, S.G. Lee, U. Paik, J. Eur. Ceram. Soc. **23**, 1427 (2003)
35. W.C. Carter, R.M. Cannon, in *Ceram. Trans.*, vol. 7, *Sintering of Advanced Ceramics*, ed. by C.A. Handwerker, J.E. Blendell, W. Kaysser (Am. Ceram. Soc., Westerville, OH, 1990) p. 137
36. C.L. Jia, K. Urban, M. Mertin, S. Hoffmann, R. Waser, Philos. Mag., A **77**, 929 (1998)
37. Y.C. Wu, C.C. Lee, D.E. McCauley, M.S.H. Chu, H.Y. Lu, J. Am. Ceram. Soc **89**, 1679 (2006)
38. Y.C. Wu, C.Y. Chen, D.E. McCauley, M.S.H. Chu, H.Y. Lu, **89**, 2213 (2006)